Transient magnetoelastic coupling in CrSBr

Youn Jue Bae,[1,*] Taketo Handa,[1] Yanan Dai,[1] Jue Wang,[1] Huicong Liu,[2] Allen Scheie,[3] Daniel G. Chica,[1] Michael E. Ziebel,[1] Andrew D. Kent,[4] Xiaodong Xu,[5] Ka Shen,[2] Xavier Roy,[1] and Xiaoyang Zhu[1,†]

[1]*Department of Chemistry, Columbia University, New York, New York 10027, USA*
[2]*The Center of Advanced Quantum Studies and Department of Physics, Beijing Normal University, Beijing 100875, China*
[3]*MPA-Q, Los Alamos National Laboratory, Los Alamos, New Mexico 87545, USA*
[4]*Department of Physics, New York University, New York, New York 10003, USA*
[5]*Department of Physics, University of Washington, Seattle, Washington 98195, USA*

(Received 17 July 2023; accepted 7 February 2024; published 1 March 2024)

Recent research has revealed remarkable properties of the two-dimensional (2D) van der Waals layered crystal CrSBr, which is both a semiconductor and an *A*-type antiferromagnet. Here we show the role of strong magnetoelastic coupling in the generation and propagation of coherent magnons in CrSBr. Time- and spatially resolved magneto-optical Kerr effect microscopy reveals two time-varying transient strain fields induced by out-of-plane transverse and in-plane longitudinal lattice displacements. These transient strain fields launch coherent wavepackets of magnons, optical and acoustic, at 24.6 ± 0.8 and 33.4 ± 0.5 GHz, respectively. These findings suggest mechanisms for controlling and manipulating coherent magnons from distinct magnetoelastic couplings in this 2D van der Waals magnetic semiconductor.

DOI: 10.1103/PhysRevB.109.104401

I. INTRODUCTION

Coherent magnons, also called spin waves, are intrinsically nonlinear due to magnetic dipole coupling [1] and their dispersions are tunable by the magnitude and directions of an external magnetic field [2]. These properties make coherent magnons ideal candidates for wave-based logic, directional coupling, and computing [3]. There are various ways to excite coherent magnons, e.g., by microwave antennas, electrical pulses, and optical pulses [4]. Among these different approaches, optical excitation provides easy access without the need for device fabrication and, when combined with optical detection, allows ultrafast tracking of spin dynamics in both time and space domains [5,6]. Optical excitation and detection also resolve low wave-vector windows that are not easily accessible with neutron scattering [7]. While optical excitation can directly transfer angular momentum to the spins via the inverse Faraday effect or the Cotton-Mouton effect, a more common mechanism is to exert transient torques on the spin system from a gradient in demagnetization field created by the excitation laser beam profile [5,8]. Alternatively, magnetoelastic coupling can also launch coherent magnons [1].

In this work, we address the mechanisms in the launch and propagation of coherent magnons in CrSBr, a two-dimensional (2D) van der Waals (vdW) material which is both a semiconductor and an *A*-type antiferromagnet (AFM), i.e., with intralayer ferromagnetic and interlayer antiferromagnetic order [9,10]. The *A*-type AFM order persists from the bulk vdW crystal to the 2D bilayer limit, with little change in the Néel temperature (132–140 K) [10]. The electronic structure is found to be strongly coupled to magnetic order in CrSBr [11], permitting the detection of coherent magnons in the microwave region by excitonic transitions in the visible-to-near-infrared region [12]. Such optical access to coherent magnons has been utilized in the tuning of magnon-exciton interactions by external magnetic field [13] and in the imaging of propagating magnons [14]. In the latter work, Sun *et al.* combined optical imaging on CrSBr with theory and concluded that long-range magnetic dipole-dipole coupling dominates the fast propagation of coherent magnons [14]. Here we focus on the launching mechanisms for coherent magnons in CrSBr. Using time-resolved magneto-optical Kerr effect (tr-MOKE) imaging, we identify two time-varying transient strain fields induced by out-of-plane transverse- and in-plane longitudinal lattice displacements, respectively. In the time-domain experimental data, we observe two distinct timescales in spin-wave decay dynamics and attribute these to two different launching mechanisms, namely the laser-induced demagnetization field and the transient strain fields that stem from the intrinsically strong magnetoelastic coupling in CrSBr.

II. EXPERIMENT

The synthesis, exfoliation, and characterization of CrSBr crystals have been detailed elsewhere [9,10]. Atomically thin flakes of CrSBr can be prepared by mechanical exfoliation onto Si/SiO_2 substrates, where the bulk magnetic structure is maintained down to the ferromagnetic (FM) monolayer with a Curie temperature $T_C = 146$ K and to the

*Present address: Department of Chemistry and Chemical Biology, Cornell University, Ithaca, NY 14853, USA; yb293@cornell.edu
†Corresponding author: xyzhu@columbia.edu

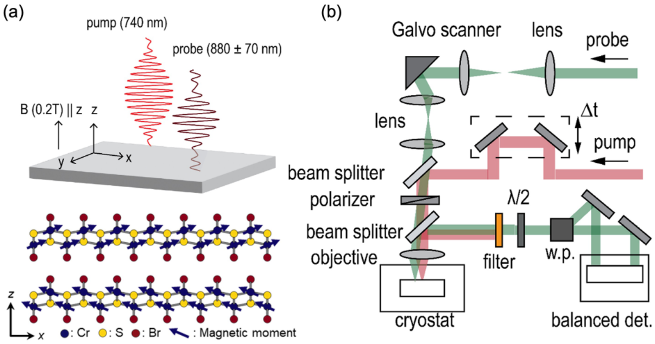

FIG. 1. Experimental setup for MOKE imaging. (a) Crystal structure of CrSBr and experimental geometry. The blue arrows represent the magnetic moments which are slightly canted away from the easy b axis in the external magnetic field. (b) Optical setup of the tr-MOKE imaging system. In all experiments, the sample temperature is 5 K and the external field is 0.2 T along z.

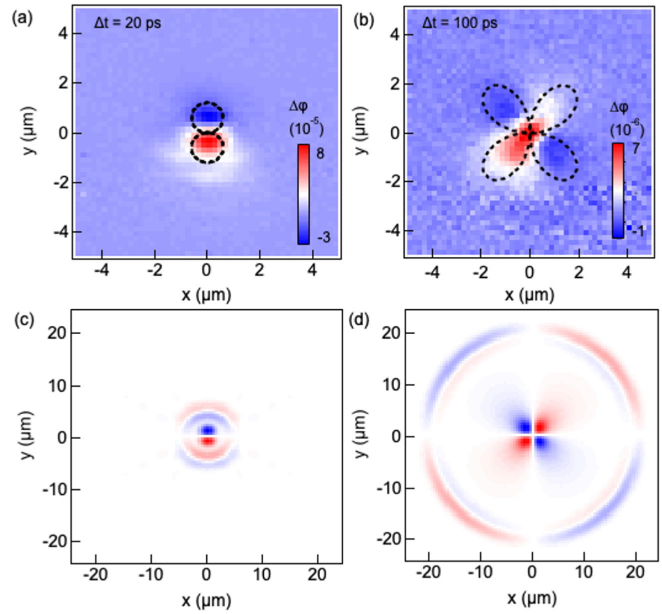

FIG. 2. Transient magnetization map reflecting magnetoelastic coupling. Experimentally measured magnetization maps from tr-MOKE at pump-probe delays (a) $\Delta t = 20$ ps and (b) $\Delta t = 100$. Calculated magnetization map from (c) shear and (d) pressure stress. See details in Supplemental Material [18].

antiferromagnetic (AFM) bilayer with a Néel temperature $T_N = 140$ K [10]. CrSBr is also a direct-gap semiconductor down to the monolayer, with an electronic gap of 1.5 eV and an excitonic gap of 1.34 eV [9]. The anisotropic nature of the exfoliated crystal allows the easy determination of crystallographic axis, c: normal to the surface (z); b: in-plane short axis (x); and a: in-plane long axis (y) [10]. The magnetic structure of CrSBr is depicted in Fig. 1(a), where the easy, intermediate, and hard axes are along the b-, a-, and c- axes, respectively. To perform tr-MOKE imaging [Figs. 1(a)–1(b)], we split the output of a Ti:sapphire regenerative amplifier (Coherent RegA, 250 kHz, 800 nm, and 100-fs pulse width) into two beams: one for the 740-nm pump generated in an optical parametric amplifier and the other for the 880-nm probe from white-light generation in a sapphire crystal with a bandpass filter of 70-nm width. The sample is mounted in a closed-cycle cryostat (Montana Instruments) to maintain a temperature of $T \sim 5$ K. We apply a magnetic field of $\mu_0 H = 0.2$ T along the c axis using a permanent magnet to tilt the spins to the out-of-plane direction necessary for the polar MOKE geometry [Fig. 1(a)]. The pump-probe pulses are delayed up to 7 ns. The probe beam is spatially separated from the pump beam by a dual-axis galvo-mirror scanning system for imaging with diffraction-limited resolution [Fig. 1(b)] [15]. The pump and the probe polarizations are along the b axis of the crystal. A balanced detection scheme is used with a lock-in amplifier where the reference signal is synchronized with the optical chopper frequency. In MOKE and transient reflectance, we detect the angle of rotation ($\Delta\phi$) and the magnitude of reflectance ($\Delta R/R$, where R is reflectance without pump and ΔR is change in reflectance by the pump).

III. RESULTS AND DISCUSSION

We optically excite an ~150-nm-thick flake of CrSBr by a pump pulse with above-gap photon energy $h\nu_1 = 1.67$ eV (pulse width 150 fs; power 1 μW; and Gaussian width 1.4 μm) and collect the spatial map of probe polarization rotation, i.e., polar MOKE imaging, by scanning the linearly polarized probe ($h\nu_2 = 1.4$ eV; pulse width 100 fs; power 0.2 μW; and Gaussian width $d \sim 1.2$ μm) as a function of pump-probe delay (Δt). The angle of polarization rotation ($\Delta\phi$) is proportional to the pump-induced changes in the out-of-plane magnetization along the z axis (Δm_z) [16]. Two representative MOKE images at pump-probe time delays of $\Delta t = 20$ and 100 ps are shown in Figs. 2(a) and 2(b), respectively. The MOKE images reveal distinct symmetries at short and long delay times. At $\Delta t = 20$ ps, the image presents a dipolar pattern in Δm_z; it is symmetric and antisymmetric with respect to the xz and xy mirror planes, respectively. At the longer delay of $\Delta t = 100$ ps, the image evolves to a quadrupolar pattern which is antisymmetric with respect to both xz and yz mirror planes. We assign the dipolar symmetry in Fig. 2(a) to transient transverse lattice displacement along the z direction and the quadrupolar symmetry in Fig. 2(b) to longitudinal lattice displacement along the in-plane x-y direction, as detailed below.

The derivation of spin-generating torque from lattice displacement has been reported by Shen and Bauer [17]. Briefly, laser excitation can transiently heat the sample and induce lattice displacement. Through magnetoelastic coupling (constant b), lattice displacement can impose shear and pressure stress to magnetizations and the direction of the induced torque depends on the direction of lattice displacement. The torque or effective field H_T resulting from longitudinal (R_l), transverse (R_t), and out-of-plane displacements (R_z) can be written as [17]

$$H_T = i\left(\frac{bk}{\hbar\gamma\mu_0}\right)[\hat{x}(R_l \sin(2\theta) + R_t \cos(2\theta)) + \hat{z}R_z \cos(\theta)], \tag{1}$$

where k is in-plane wave vector; b is magnetoelastic coupling constant; γ is gyromagnetic ratio; θ is in-plane angle between the equilibrium magnetic moment and k; μ_0 is Bohr

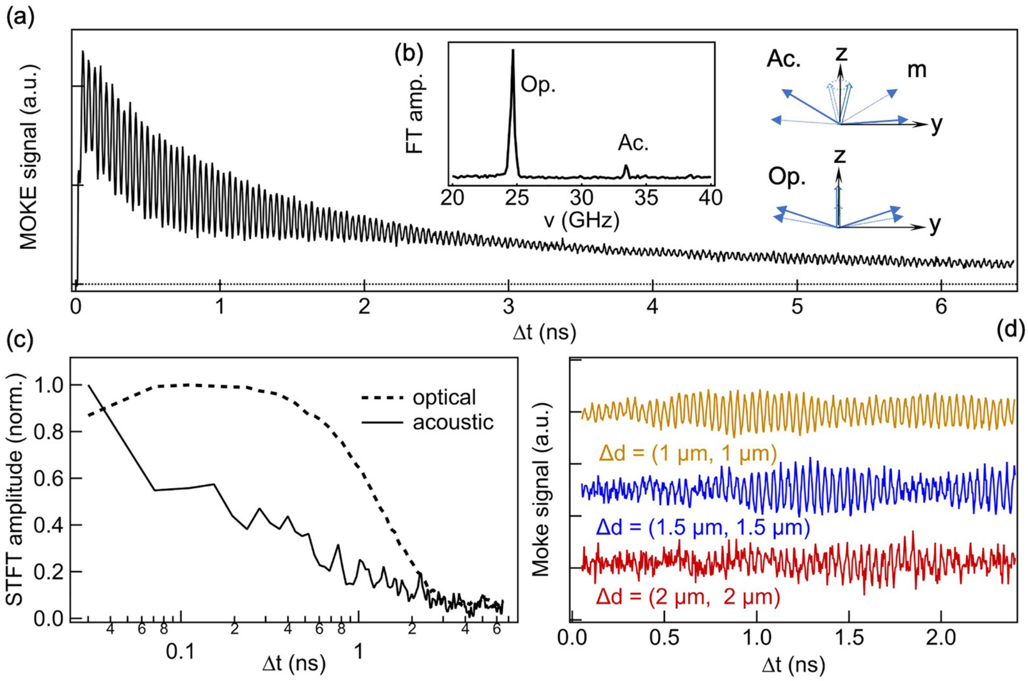

FIG. 3. Temporal dynamics of optical and acoustic magnon modes. (a) The kinetic trace of tr-MOKE signal with spatially overlapping pump-probe. The inset (b) shows the Fourier transform and illustrations of normal modes of acoustic and optical magnons. (c) Short-time Fourier transform (STFT) of (a) obtained with a time window of 50 ps; (d) The kinetic traces of tr-MOKE signal obtained with the probe spatially offset by the indicated coordinates and the pump at (0 μm, 0 μm).

magneton; $\hbar$ is the Planck constant; $\hat{x}$ and $\hat{z}$ are unit vectors in x and z directions, respectively. The light propagation and the external magnetic field B_0 are both along the z axis. Using parameters for CrSBr, we simulate the magnetization maps resulting from magnetoelastic coupling in the presence of shear stress due to an in-plane longitudinal phonon mode and pressure stress from an out-of-plane transverse phonon mode, respectively. The simulated patterns induced by the shear and pressure stress [Figs. 2(c) and 2(d)] show the same symmetries as the experimental data at 20 and 100 ps, respectively. As a result, we assign the distinct symmetries in magnetization maps as arising from in-plane longitudinal and out-of-plane transverse lattice displacements, respectively (Fig. S1, in the Supplemental Material [18]; see also Refs. [19,20] therein). Note that in addition to the dipolar and quadrupolar patterns, the simulation also reveals circular patterns at larger distances with the same symmetries. These circular patterns at longer distances are not observed in Figs. 2(a) and 2(b), likely resulting in part from insufficient experimental sensitivity and in part from incoherent lattice displacements from multiple phonon modes involved.

We find from time-domain measurements that the fast decay in shear stress due to an in-plane longitudinal phonon mode may contribute to an additional channel for the delayed launch of coherent magnons. Figure 3(a) shows time-dependent MOKE signal obtained from spatially overlapping pump-probe pulses. The presence of coherent magnons is obvious in the periodic oscillations of the magnetization. We carry out Fourier transform (FT) directly from the time-domain signal [Fig. 3(b)], which reveals two magnon modes at 24.6 ± 0.8 GHz (time period $\tau_1 = 42$ ps) and 33.4 ± 0.5 GHz (time period $\tau_2 = 30$ ps), assigned to the optical (Op) and acoustic (Ac) modes of the interlayer AFM magnon, respectively. This assignment originates from the specific anisotropy of the system in the presence of an external magnetic field along the c axis [12,13], as detailed in Fig. S2 [18]. The full width at half maximum of the two modes are 0.8 and 0.5 GHz for optical and acoustic modes, respectively. The narrow linewidth in the frequency domain originates from long-lived coherence in the time-domain signal, indicating low decoherence rates. From antiferromagnetic resonance spectroscopy (AFRS), we find that the intrinsic damping rates of the two modes at momentum-vector $k \sim 0$ are of the order of 0.1 GHz (Fig. S3 and Fig. S4) [18]. However, optically launched coherent magnons possess finite momentum-vector distributions as determined by the finite size of the pump laser beam (see below). The momentum-vector distribution gives rise to broader width (from decoherence) than that determined in AFRS.

By taking the short-time Fourier transform (STFT, time window 50 ps) of the data in Fig. 3(a), we find that the frequencies of the two magnon modes remain constant but their amplitudes [Fig. 3(c)] show distinctly different time dependences. While the amplitude of the acoustic magnon mode (solid curve) decays monotonically, with a time constant of ~0.3 ns, that of the optical magnon mode (dashed curve) shows an additional small rise in <80 ps and decays on a much longer timescale of ~2 ns. The timescale of the additional rise in the optical magnon model [Fig. 3(c)] is of the same order as the decay time of the in-plane longitudinal phonon mode inferred from the MOKE images in Fig. 2. If this decay occurs on sufficiently short timescales, $t \leqslant \tau_1$

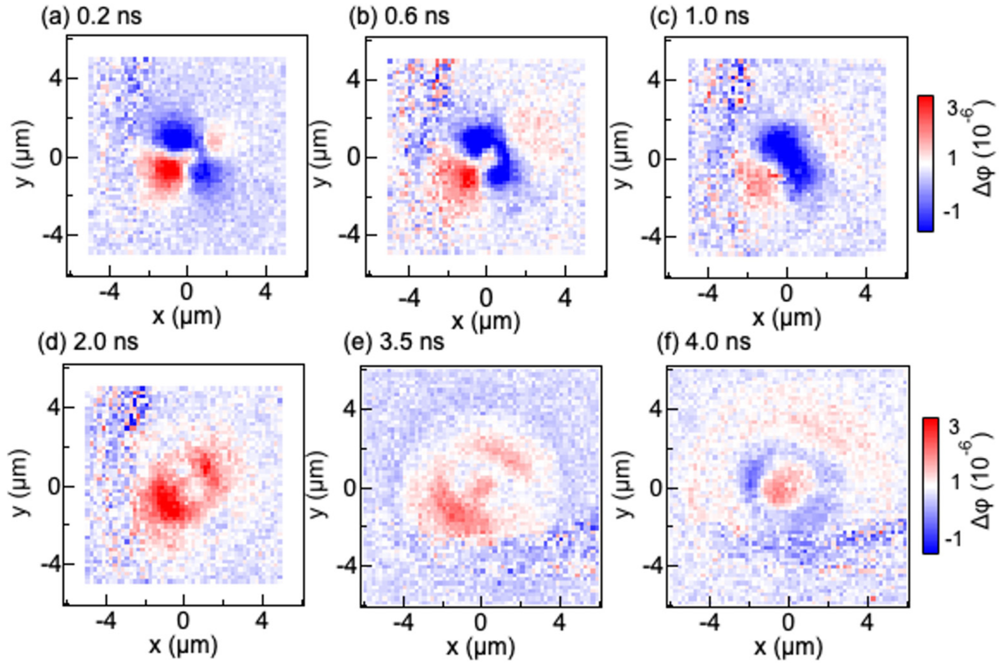

FIG. 4. Spatial symmetries of magnetization from tr-MOKE images. The images were obtained at pump-probe delays of $\Delta t =$ (a) 0.2 ns, (b) 0.6 ns, (c) 1.0 ns, (d) 2.0 ns, (3) 3.5 ns, and (f) 4.0 ns following diffraction limited excitation at x, $y = 0, 0$.

(=42 ps), the resulting transient torque may additionally launch a coherent wavepacket of the optical magnons at 24 GHz, thus accounting for the small early-time rise in the amplitude of this mode [Fig. 3(c)]. This timescale is in the range for the relaxation of optical phonons to acoustic phonons [21]. It is likely that the transient torque comes from the conversion of longitudinal optical (LO) phonons to out-of-plane transverse acoustic (TA) phonons.

Supporting the above interpretation, we note the presences of beating patterns in time-domain traces. There are minima in the oscillating amplitudes at $\Delta t = 3$–4 ns for the spatially overlapping pump-probe data in Fig. 3(a), and at $\Delta t \sim 1.6$ ns (brown) and $\sim$1.9 ns (blue) for spatially displaced pump-probe at $(\Delta x,\ \Delta y) = (1\ \mu\text{m},\ 1\ \mu\text{m})$ and (1.5 μm, 1.5 μm), respectively, in Fig. 3(d); note that for $(\Delta x,\ \Delta y) = (2\ \mu\text{m},\ 2\ \mu\text{m})$, the beating pattern is not well resolved due to the low signal-to-noise ratio (red). These beating patterns suggest the presence of closely spaced frequency components. The initial Gaussian spatial profile of the focused excitation pulse creates a demagnetization field whose gradient launches coherent magnon wavepackets in a momentum vector range of approximately 0–$1/\sigma$, where σ is the Gaussian width ($= 1.2\ \mu$m in the present case) [22,23]. We estimate from these momentum windows the corresponding frequency range of $\sim$1 GHz based on the dispersions of the optical magnon mode reported by Sun *et al.* [14]. For the additional delayed launch of the coherent magnon wavepacket, the spatial extent of the torque is expected to be larger than that of the initial laser excitation spot due to the diffusion of carriers and phonons. As a result, we expect the momentum-vector range for the additional coherent phonon wavepacket to be narrower than that of the initially launched wavepacket. The difference in the momentum-vector (frequency-) ranges of the wavepackets provides a plausible explanation for the beating patterns. We extend the time-domain MOKE data.imaging in Figs. 2(a) and 2(b) to longer timescales (Fig. 4). Contrary to the fast-decaying shear stress responsible for the dipolar magnitization pattern, the pressure stress associated with the quadrupolar pattern persists on longer timescales, $\Delta t = 0.2$, 0.6, and 1.0 ns in Figs. 4(a), 4(b), and 4(c), respectively. At longer times, $\Delta t \geqslant 2.0$ ns, the magnetization pattern becomes increasingly isotropic (circular) [$\Delta t = 2.0$–4.0 ns, Figs. 4(d)–4(f)]. We determine group velocities of the two coherent magnon modes along the specific crystal axes by displacing the probe beam with respect to the pump beam and obtain time-domain traces similar to those in Fig. 3(d). We then take the STFT with a time window of 50 ps and identify the Δt at maximum STFT amplitude. From the analysis, we obtain group velocities from time-resolved MOKE data to be 1.3 ± 0.2 km/s along both a- and b axes for the optical magnon mode. For the acoustic mode, the group velocity is 3.7 ± 0.4 km/s along the a axis and not measurable along the b axis. These results are in good agreement with prior measurements based on exciton sensing [12]. Such isotropic propagation of the optical magnon mode at 24 GHz has been identified by Sun *et al.* as originating from long-range dipolar interactions in the layered CrSBr [14]. Those authors concluded that the dipolar mechanism should be responsible for the fast and isotropic transport of magnons in vdW magnets in general.

IV. SUMMARY

We identify laser-induced transient strain field in launching coherent magnons, an acoustic and an optical mode, in CrSBr. From spatially and temporally resolved MOKE measurements, we identify two types of transient torque due to magnetoelastic coupling from longitudinal and transverse lattice displacements, leading to distinct magnetization symmetries. The former is short-lived (∼20 ps), whereas the latter slowly decays over the timescale of nanoseconds. The decay of the short-lived longitudinal phonon may add to an additional but delayed mechanism for the launching of the coherent wavepacket of the optical magnon. These results provide evidence for strong magnetoelastic coupling, which in our measurement is in the nonresonant region, as the acoustic phonon frequencies [24] in the momentum range determined by the spatial extent of the laser excitation spot are an order of magnitude lower than those of the magnons measured here.

Magnetoelastic coupling has been probed extensively before in AFM materials [25], such as the three-dimensional NiO [26] and α-MnTe [27]. Conventionally, magnetoelastic coupling stems from modulation in magnetic anisotropy or spin-orbit coupling (SOC) interactions by collective lattice oscillations. In CrSBr, magnetic anisotropy stems from anisotropic superexchange interactions mediated by Br, where the SOC of Br generates a magnetocrystalline anisotropy larger than that of single-ion anisotropy of Cr(III). The large magnetoelastic coupling has been observed in two other 2D antiferromagnets: in $FePS_3$, but primarily comes from the single-ion anisotropy of Fe(II) [28]. Magnetoelastic coupling has also been reported to be important to a 2D stripe AFM, CrOCl [29]. We posit that their low dimensionality conserves spin interactions to in-plane directions and may play a crucial role in enhancing magnetoelastic coupling. Furthermore, in CrSBr which possesses strong magnetoelectronic and magnetoelastic coupling due to the simultaneous presence of magnetic and semiconducting properties, their common connection to the electronic structure may play a role in enhancing magnetoelastic coupling.

ACKNOWLEDGMENTS

The spectroscopic and imaging work was supported by the Materials Science and Engineering Research Center (MRSEC) through NSF Grant No. DMR-2011738 to X.Z. and X.R. The synthesis of the CrSBr crystals was supported as part of Programmable Quantum Materials, an Energy Frontier Research Center funded by the U.S. Department of Energy (DOE), Office of Science, Basic Energy Sciences (BES), under Award No. DE-SC0019443 to X.R., X.Z., and X.X. The magnetic resonance spectroscopy work was supported by the Air Force Office of Scientific Research under Grant FA9550-19-1-0307 to A.D.K. The magnetoelastic coupling calculation is supported by the National Natural Science Foundation of China (Grants No.11974047 and No.12374100) and the Fundamental Research Funds for the Central Universities to K.S.

[1] A. G. Gurevich and G. A. Melkov, *Magnetization Oscillations and Waves*, 1st ed. (CRC press, London, 1996).

[2] A. V. Chumak, V. I. Vasyuchka, A. A. Serga, and B. Hillebrands, Magnon spintronics, Nat. Phys. **11**, 453 (2015).

[3] Q. Wang *et al.*, A magnonic directional coupler for integrated magnonic half-adders, Nat. Electron. **3**, 765 (2020).

[4] A. A. Serga, A. V. Chumak, and B. Hillebrands, YIG magnonics, J. Phys. D: Appl. Phys. **43**, 264002 (2010).

[5] A. Kirilyuk, A. V. Kimel, and T. Rasing, Ultrafast optical manipulation of magnetic order, Rev. Mod. Phys. **82**, 2731 (2010).

[6] M. van Kampen, C. Jozsa, J. T. Kohlhepp, P. LeClair, L. Lagae, W. J. M. de Jonge, and B. Koopmans, All-optical probe of coherent spin waves, Phys. Rev. Lett. **88**, 227201 (2002).

[7] T. Sebastian, K. Schultheiss, B. Obry, B. Hillebrands, and H. Schultheiss, Micro-focused Brillouin light scattering: Imaging spin waves at the nanoscale, Front. Phys. **3**, 35 (2015).

[8] P. Němec, M. Fiebig, T. Kampfrath, and A. V. Kimel, Antiferromagnetic opto-spintronics, Nat. Phys. **14**, 229 (2018).

[9] E. J. Telford *et al.*, Layered antiferromagnetism induces large negative magnetoresistance in the van der Waals semiconductor CrSBr, Adv. Mater. **32**, 2003240 (2020).

[10] K. Lee, A. H. Dismukes, E. J. Telford, R. A. Wiscons, X. Xu, C. Nuckolls, C. R. Dean, X. Roy, and X. Zhu, Magnetic order and symmetry in the 2D semiconductor CrSBr, Nano Lett. **21**, 3511 (2021).

[11] N. P. Wilson *et al.*, Interlayer electronic coupling on demand in a 2D magnetic semiconductor, Nat. Mater. **20**, 1657 (2021).

[12] Y. J. Bae *et al.*, Exciton-coupled coherent magnons in a 2D semiconductor, Nature (London) **609**, 282 (2022).

[13] G. M. Diederich *et al.*, Tunable interaction between excitons and hybridized magnons in a layered semiconductor, Nat. Nanotechnol. **18**, 23 (2023).

[14] Y. Sun, F. Meng, C. Lee, A. Soll, H. Zhang, R. Ramesh, J. Yao, Z. Sofer, and J. Orenstein, Universal spin wavepacket transport in van der Waals antiferromagnets, arXiv:2309.03278.

[15] J. Wang *et al.*, Diffusivity reveals three distinct phases of interlayer excitons in MoSe2/WSe2 heterobilayers, Phys. Rev. Lett. **126**, 106804 (2021).

[16] J. Wang, Time-resolved magneto-optical spectroscopy, *Optical Techniques for Solid-State Materials Characterization* (CRC Press, Boca Raton, 2016), pp. 242–245.

[17] K. Shen and G. E. W. Bauer, Theory of spin and lattice wave dynamics excited by focused laser pulses, J Phys D: Appl Phys **51**, 224008 (2018).

[18] See Supplemental Material at http://link.aps.org/supplemental/10.1103/PhysRevB.109.104401 for additional data and analysis.

[19] T. L. Gilbert, A phenomenological theory of damping in ferromagnetic materials, IEEE Trans. Magn. **40**, 3443 (2004).

[20] H. T. Simensen, R. E. Troncoso, A. Kamra, and A. Brataas, Magnon-polarons in cubic collinear antiferromagnets, Phys. Rev. B **99**, 064421 (2019).

[21] J. Shah, *Ultrafast Spectroscopy of Semiconductors and Semiconductor Nanostructures* (Springer Science & Business Media, New York, 2013), Vol. 115.

[22] Y. Au, M. Dvornik, T. Davison, E. Ahmad, P. S. Keatley, A. Vansteenkiste, B. Van Waeyenberge, and V. V. Kruglyak, Direct excitation of propagating spin waves by focused ultrashort optical pulses, Phys. Rev. Lett. **110**, 097201 (2013).

[23] A. Kamimaki, S. Iihama, Y. Sasaki, Y. Ando, and S. Mizukami, Reciprocal excitation of propagating spin waves by a laser pulse and their reciprocal mapping in magnetic metal films, Phys. Rev. B **96**, 014438 (2017).

[24] L. Talirz, S. Kumbhar, E. Passaro, A. V. Yakutovich, V. Granata, F. Gargiulo, M. Borelli, M. Uhrin, S. P. Huber, and S. Zoupanos, Materials cloud, a platform for open computational science, Sci. Data **7**, 299 (2020).

[25] V. Baltz, A. Manchon, M. Tsoi, T. Moriyama, T. Ono, and Y. Tserkovnyak, Antiferromagnetic spintronics, Rev. Mod. Phys. **90**, 015005 (2018).

[26] D. Bossini, M. Pancaldi, L. Soumah, M. Basini, F. Mertens, M. Cinchetti, T. Satoh, O. Gomonay, and S. Bonetti, Ultrafast amplification and nonlinear magnetoelastic coupling of coherent magnon modes in an antiferromagnet, Phys. Rev. Lett. **127**, 077202 (2021).

[27] K. Deltenre, D. Bossini, F. B. Anders, and G. S. Uhrig, Lattice-driven femtosecond magnon dynamics in $\alpha-$ MnTe, Phys. Rev. B **104**, 184419 (2021).

[28] Q. Zhang, M. Ozerov, E. V. Boström, J. Cui, N. Suri, Q. Jiang, C. Wang, F. Wu, K. Hwangbo, and J.-H. Chu, Coherent strong-coupling of terahertz magnons and phonons in a van der Waals antiferromagnetic insulator, arXiv:2108.11619.

[29] P. Gu, Y. Sun, C. Wang, Y. Peng, Y. Zhu, X. Cheng, K. Yuan, C. Lyu, X. Liu, and Q. Tan, Magnetic phase transitions and magnetoelastic coupling in a two-dimensional stripy antiferromagnet, Nano Lett. **22**, 1233 (2022).